

# Is the plateau state in GRS 1915+105 equivalent to canonical hard states?

Pieter van Oers<sup>1,2</sup>, Sera Markoff<sup>1</sup>, Dipankar Maitra<sup>1,3</sup>, Farid Rahoui<sup>4,5,6</sup>,  
Michael Nowak<sup>7</sup>, Jörn Wilms<sup>8</sup>, Alberto J. Castro-Tirado<sup>9</sup>, Jerome Rodriguez<sup>4</sup>,  
Vivek Dhawan<sup>10</sup>, and Emilios Harlaftis<sup>11\*</sup>

<sup>1</sup> *Astronomical institute “Anton Pannekoek”, University of Amsterdam, Science Park 904, 1098 XH, The Netherlands*

<sup>2</sup> *New affiliation: School of Physics & Astronomy, University of Southampton, Highfield, Southampton SO17 1BJ, United Kingdom*

<sup>3</sup> *New affiliation: Department of Astronomy, University of Michigan, 500 Church St., Ann Arbor, MI 48109, USA*

<sup>4</sup> *Laboratoire AIM, CEA/IRFU, Université Paris Diderot, CNRS/INSU, CEA Saclay, DSM/IRFU/SAP, F-91191 Gif sur Yvette, France*

<sup>5</sup> *AstroParticule & Cosmologie (APC) / Université Paris VII / CNRS / CEA / Observatoire de Paris, Bât. Condorcet,*

*10 rue Alice Domon et Léonie Duquet, 75205 Paris Cedex 13, France*

<sup>6</sup> *Department of Astronomy & Harvard-Smithsonian Center for Astrophysics, Harvard University, 60 Garden street, Cambridge, MA 02138, USA*

<sup>7</sup> *Kavli Institute for Astrophysics and Space Research, Massachusetts Institute of Technology, Cambridge, USA*

<sup>8</sup> *Dr. Karl Remeis-Sternwarte, Astronomisches Institut, Universität Erlangen-Nuremberg, Sternwartstr. 7, 96049, Germany*

<sup>9</sup> *Instituto de Astrofísica de Andalucía (IAA-CSIC), Glorieta de la Astronomía s/n, 18008 Granada, Spain*

<sup>10</sup> *National Radio Astronomy Observatory, 10003 Lopezville Road, Socorro, NM 87801, USA*

<sup>11</sup> *Institute of Space Applications and Remote Sensing, National Observatory of Athens, PO Box 20048, Athens 11810, Greece*

August 9, 2021

## ABSTRACT

GRS 1915+105 is a very peculiar black hole binary that exhibits accretion-related states that are not observed in any other stellar-mass black hole system. One of these states, however – referred to as the plateau state – may be related to the canonical hard state of black hole X-ray binaries. Both the plateau and hard state are associated with steady, relatively lower X-ray emission and flat/inverted radio emission, that is sometimes resolved into compact, self-absorbed jets. However, while generally black hole binaries quench their jets when the luminosity becomes too high, GRS 1915+105 seems to sustain them despite the fact that it accretes at near- or super-Eddington rates. In order to investigate the relationship between the plateau and the hard state, we fit two multi-wavelength observations using a steady-state outflow-dominated model, developed for hard state black hole binaries. The data sets consist of quasi-simultaneous observations in radio, near-infrared and X-ray bands. Interestingly, we find both significant differences between the two plateau states, as well as between the best-fit model parameters and those representative of the hard state. We discuss our interpretation of these results, and the possible implications for GRS 1915+105’s relationship to canonical black hole candidates.

**Key words:** Black hole physics – accretion, accretion discs – radiation mechanisms: general – X-rays: binaries – galaxies: active – galaxies: jets

## 1 INTRODUCTION

The microquasar GRS 1915+105 was discovered on 15 August 1992, by the WATCH all-sky monitor, aboard the Russian GRANAT satellite (Castro-Tirado, Brandt, & Lund 1992; Castro-Tirado et al. 1994). It is a hard X-ray transient located in the constellation of Aquila, at  $l = 45.37^\circ$ ,  $b = -0.22^\circ$ , and was the first stellar mass accreting black

hole binary (BHB) discovered to exhibit superluminal velocities in its radio emitting-ejecta (Mirabel & Rodríguez 1994). The obvious parallels to the jets in Active Galactic Nuclei (AGN) led to this source being classified as a “microquasar” (Mirabel & Rodríguez 1998). Subsequent observations with instruments onboard the *Rossi X-ray Timing Explorer (RXTE)* have revealed a richness in variability, distinguishing GRS 1915+105 from every other known BHB, over which astronomers are still puzzling to this day.

\* In Memoriam

The longer term X-ray variability exhibits “dipping”

that is thought to be associated with the recession and regeneration of the inner parts of the accretion disc, perhaps caused by the onset of thermal-viscous instabilities (Belloni et al. 1997b,a). Other models have interpreted the spectral changes as resulting from the disappearance of the corona (Chaty 1998; Rodriguez et al. 2008a,b), or from the dissipation of magnetic energy via magneto-hydrodynamical plasma processes (e.g. Tagger et al. 2004).

Beyond the dipping behaviour, Belloni et al. (2000) were able to classify all variability patterns stretching over more than a year into only twelve classes (Klein-Wolt et al. 2002; Hannikainen et al. 2005 later identified two more classes), based on colour-colour diagrams and light curves. Ten of these twelve classes can be understood as the interplay of two or three of three basic states, designated as states A, B and C. The remaining two classes,  $\phi$  and  $\chi$ , do not show state transitions and appear exclusively within states A and C respectively. State A displays the highest flux and the softest spectrum while state C displays the lowest flux and the hardest spectrum. Although state B never lasts for more than a few hundred seconds,  $\phi$  and  $\chi$  episodes can persist for days or short intervals of  $< 100$  s.

Aside from the existence of so many distinct accretion states, GRS 1915+105 appears similar to other BHBs. Thus there has been much discussion (e.g. Reig, Belloni, & van der Klis 2003) about the extent to which any of the states found in GRS 1915+105 correspond to the “canonical” states (see e.g. Homan & Belloni 2005; Remillard & McClintock 2006 for definitions) found in the average BHB. BHBs generally spend the majority of their time in the Hard State (HS), which is associated with a low accretion rate, a hard X-ray power law component with photon index  $1.4 \leq \Gamma \leq 2.1$ , and steady radio emission with an optically thick, flat-to-inverted spectrum. Sources that persist in the HS for several weeks generally show clear correlations between the radio and X-ray luminosities ( $L_R \propto L_X^{0.7}$ ) (Corbel 2000; Corbel et al. 2003; Gallo, Fender, & Pooley 2003). More recently, evidence for a similar correlation between the near-infrared (NIR) and X-ray bands has also been found (Russell et al. 2006; Coriat et al. 2009).

Similar to the other BHBs, GRS 1915+105 also displays periods of relatively hard, steady X-ray emission, but in contrast to the HS, only for about half the observation time (Trudolyubov 2001). Belloni et al. (2000) identify these intervals of decreased variability with long C state episodes. The subset of state C/ class  $\chi$  observations that are radio-bright are referred to as the *plateau* state (ibid.), but elsewhere have variously been referred to as the radio-loud, radio-plateau or radio loud low/hard X-ray state (Muno et al. 2001), the type II hard steady state (Trudolyubov 2001) and  $\chi_{RL}$  (Naik & Rao 2000).

The plateau state was first described by Foster et al. (1996) and its description was later refined in Fender et al. (1999). The state can assert itself in a period as short as a day and is characterised by a decrease in X-ray flux density and an increase in radio flux density to a steady value, typically  $\sim 10 - 100$  mJy. Ample evidence supports the fact that the plateau state X-ray and radio luminosities are indeed correlated, with an increasing delay from X-ray to infrared (IR) to radio emission (e.g. Klein-Wolt et al. 2002). As in the HS the plateau radio spectrum is optically thick, and AU-scale self-absorbed compact jets have been spatially

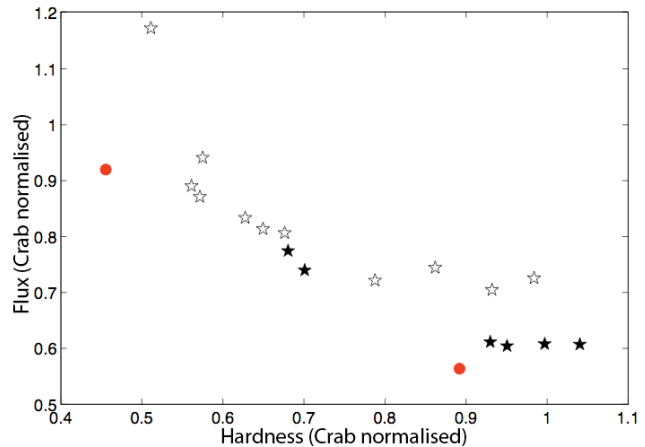


**Figure 1.** HID comparing our observations (filled circles) to the plateau states from Belloni et al. (2000) (data courtesy of T. Belloni; open stars are  $\chi_1$ , closed stars are  $\chi_3$ ). The soft, higher-luminosity red dot is ObsID 90105-07-02-00, the lower is ObsID 40403-01-09-00. The plot shows the hardness and flux, normalised to Crab units, calculated by taking the ratio and the sum of the *RXTE* PCU2 rates in two bands: channel 0-35 ( $\sim 2 - 15$  keV) and 36-49 ( $\sim 16 - 21$  keV). Each band is divided by the Crab rate in the same band, on the same day, simulating a photon index of 2.1 and utilising a normalisation of  $10 \text{ photons cm}^{-2} \text{ s}^{-1} \text{ keV}^{-1}$  at 1 keV.

resolved using Very Long Baseline Interferometry (VLBI) (Dhawan, Mirabel, & Rodríguez 2000; Fuchs et al. 2003b). Another marker of the plateau state comes from timing analyses, where 1-10 Hz quasi-periodic oscillations (QPOs) are present (Rao et al. 2000). The exact frequency of these QPOs appears to be inversely correlated with the radio and soft X-ray flux (Rau & Greiner 2003; Rodriguez et al. 2002).

In line with these arguments, it is tempting to identify the plateau state as GRS 1915+105’s analog of the HS. However, although the plateau state and the HS share many similarities, it does display some distinct properties that cannot be ignored. For instance, while the BHBs in the HS usually have a luminosity of  $\lesssim 10\% L_{\text{Edd}}$ , the average luminosity observed in the plateau state is  $\sim L_{\text{Edd}}$ . Moreover, the plateau X-ray photon index is never very hard, with  $\Gamma \sim 1.8 - 2.5$  (Fender & Belloni 2004). Finally, Reig, Belloni, & van der Klis (2003) argue that the canonical HS is never seen in GRS 1915+105 because a power-law tail (with no exponential cut off) is always present in the plateau state hard X-rays. Although the origin of such tails in the softer states of canonical BHBs is still under debate, it is generally not associated with the HS.

In this work, we seek to make a more quantitative comparison between the plateau state found in GRS 1915+105 and the HS found in more typical black holes, in the context of an outflow-dominated model that has successfully described broadband data from several BHBs. In Section 2 we describe the multi-wavelength data and the reduction methods. We discuss what physical parameters we use for modelling and why in Section 3 and the model itself, together with the results in Section 4. We put our work into context with the findings of others in Section 5, before drawing our final conclusions in Section 6.

**Table 1.** Observations included in dataset 1 and 2, with *RXTE* ObsID 40403-01-09-00 and 90105-07-02-00 respectively. The *H* and *K* bands, obtained using the Cooled Grating Spectrometer at UKIRT, are at 1.455-2.094 and 1.906-2.547  $\mu\text{m}$ , respectively (*J* band measurements were also done, but these are unusable due to high interstellar extinction). The *K* band observation in dataset 2 was done (more than half a day before ObsID 90105-07-02-00) with the ANDICAM at CTIO. The GBI measurements are 2.25 & 8.3 GHz and the flux densities used are 30 sec vector scan averages. The Ryle telescope operates at 15 GHz and the flux density used is the average of  $\sim 13$  ks worth of five minute integrations.

| Dataset 1 1999 July 8 / MJD 51367 |             |              |            |           | Dataset 2 2005 April 13 / MJD 53473 |            |          |          |
|-----------------------------------|-------------|--------------|------------|-----------|-------------------------------------|------------|----------|----------|
| Band                              | Instrument  | MJD start    | UTC        | Duration  | Instrument                          | MJD start  | Time     | Duration |
| X-ray                             | <i>RXTE</i> | 51367.2737   | 06:34:13   | 14435 sec | <i>RXTE</i>                         | 53473.054  | 01:09:05 | 6769 sec |
| NIR                               | UKIRT       | ( <i>H</i> ) | 51367.4821 | 11:34:10  | CTIO ( <i>K</i> )                   | 53472.3216 | 07:43:06 | 25 min   |
|                                   |             | ( <i>K</i> ) | 51367.8216 | 07:56:59  |                                     |            |          |          |
| Radio                             | GBI         | 51367.371    | 09:02:53   | 30 sec    | Ryle                                | 53473.098  | 02:21:07 | 219 min  |

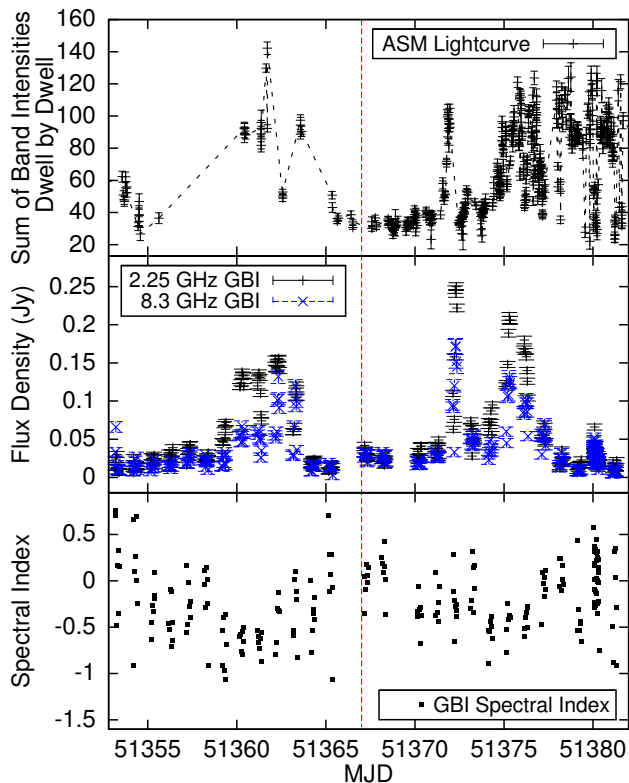


**Figure 2.** GRS 1915+105 X-ray and radio lightcurves for the 1999 data set. Also the radio spectral index, as measured by the Green Bank Interferometer is shown. The red dashed line indicates the time of the *RXTE* observation.

## 2 OBSERVATIONS AND DATA REDUCTION

Based on the lightcurves and its position in the Hardness Intensity Diagram (HID) diagram (see Figures 1, 2 & 3), GRS 1915+105 was in a class  $\chi$  state on July 8th 1999 (dataset 1) and April 13th 2005 (dataset 2). The presence of a 2-5 Hz QPO on both occasions (see Figure 4) corroborates this fact. During the 1999 episode, quasi-simultaneous radio and near-infrared observations were performed using the United Kingdom Infra-Red Telescope (UKIRT) and the Green Bank Interferometer (GBI). The 2005 dataset also holds observations of the Cerro Tololo Inter-American Observatory (CTIO) and Ryle telescope. Details on the observations and reduction methods are found in the individual

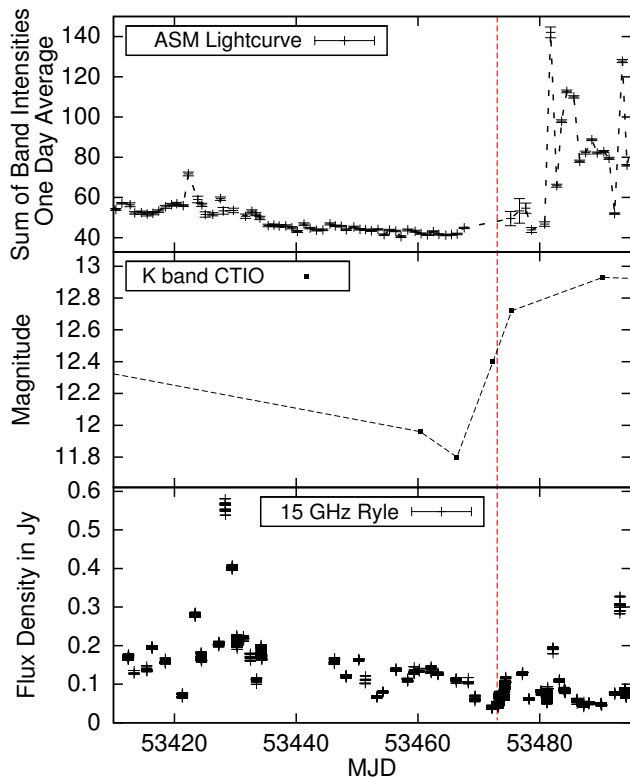


**Figure 3.** GRS 1915+105 X-ray and radio lightcurves for the 2005 data set. The radio lightcurve was measured by the Ryle Telescope (Pooley & Fender 1997). The red dashed line indicates the time of the *RXTE* observation.

Sections and Table 1. The 2005 *RXTE* data is also extensively analysed and discussed in Rodriguez et al. (2008a,b)

### 2.1 X-ray: *RXTE* data reduction

We use data from two instruments on board the *RXTE*: the Proportional Counter Array (PCA; Jahoda et al. 2006) and the High Energy X-ray Timing Experiment (HEXTE; Rothschild et al. 1998). The X-ray data have been reduced using *HEASOFT*, version 6.3.1., applying standard extraction criteria: a pointing offset of  $< 0.01^\circ$  from the nominal source position, and a source elevation of  $> 10^\circ$ . The exclusion time for the South Atlantic Anomaly (SAA), however, was only 10 min, as GRS 1915+105 is a very bright source. For the

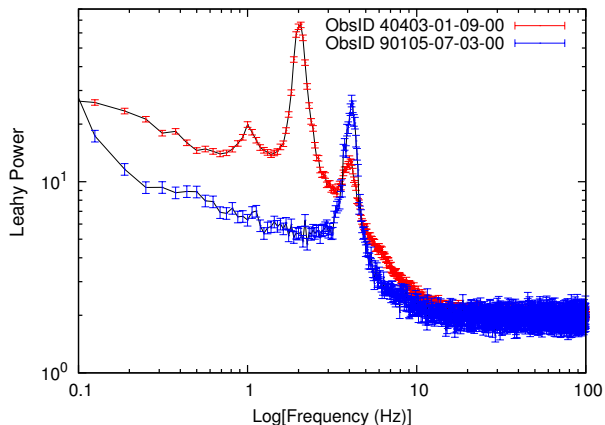


**Figure 4.** Normalised (following Leahy et al. 1983) power density spectra showing the type-C QPOs in the X-rays for both datasets, indicating the observations are plateau state. (Courtesy of P. Soleri)

same reason we disregarded the top layer and imposed a maximum “electron ratio” of 2, to take into account contamination by source photons. All HEXTE data products were dead-time corrected. Correction for the PCA dead-time was also carried out; PCU 4 was inactive for half of the 1999 observation, while during the other half, both PCU 1 and 4 were inactive. The 2005 observation was done with PCU 0 and 2 only. Due to uncertainties in the first four PCA channels, we only include PCA data above 3 keV. The PCA calibration falls off rapidly above  $\sim 25$  keV and since HEXTE provides reliable data for energies  $\gtrsim 20$  keV we ignored the PCA data above 22 keV. For the PCA, standard2f mode data were used. The PCA background was modelled using the `pca.bkgd.cmbrightv1e.eMv20051128` model. Only HEXTE data above 20 keV were used due to the uncertainty of the response matrix below these energies. At high energies, the spectrum was ignored above 200 keV. We rebinned the X-ray data to a minimum S/N of 4.5.

## 2.2 NIR: UKIRT data reduction and CTIO

On 1999 July 08, medium-resolution spectroscopic observations of GRS 1915+105 were performed with the Cooled Grating Spectrometer (CGS4) mounted on the United Kingdom InfraRed Telescope (UKIRT, P.I. Harlaftis). Twenty-four spectra in the B1 and eighteen in the B2 filters were acquired, each time at two nodding positions, giving a total exposure time of 1260 s in B1 and 1080 s in B2. Moreover, the telluric standard HD 176232, a F0p main sequence star, was observed in the same conditions.

All the spectra were reduced with *IRAF* through bad pixel correction, flat fielding, and sky subtraction. The target spectra were then extracted and wavelength calibrated by extracting, in the same condition, krypton and argon spectra in B1 and B2, respectively. They were combined and telluric feature-corrected through the division by the standard star spectrum. We finally multiplied the corrected spectrum by a F0V star one from the ISAAC synthetic spectra

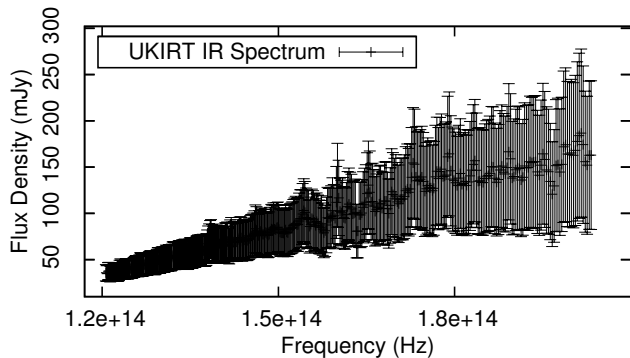


**Figure 5.** NIR spectrum of the 1999 data set

library<sup>1</sup>, resampled to the CGS4 resolution and flux-scaled to match the HD 176232 magnitudes in H and Ks. The uncertainty of the flux calibration obtained this way is about 5%.

The spectra were then dereddened using the extinction laws given in (Cardelli, Clayton, & Mathis 1989) and (Chiar & Tielens 2006), assuming a hydrogen column density of  $N_{\text{H}}=3.5 \times 10^{22} \text{ cm}^{-2}$ , i.e.  $A_{\text{V}}=19.6 \pm 1.7$  (Chapuis & Corbel 2004). The errors resulting from using the two different methods were then added in quadrature. The overall propagated uncertainties, combining flux calibration and dereddening, represent about 20% of the flux. The final spectrum is shown in Figure 5.

The UKIRT spectrum included in dataset 1 was also rebinned, because the spectral resolution is well beyond what we need for continuum fitting (see Section 4).

The 12.40 mag K band point in dataset 2 was taken using the CTIO 1.3m telescope using the ANDICAM (A Novel Double-Imaging CAMERA) detector (Neil, Bailyn, & Cobb 2007). It was dereddened using the same method as the UKIRT data. However we chose the error bars to account for the fact that GRS 1915+105 may have been approaching a state transition: The source magnitude varies from 11.8 to 12.72 in about 9 days (see Figure 3), suggesting a dereddened flux density of  $67.85 \pm 27.25$  mJy. On MJD 53473 we also see the flux in radio increasing (see below).

## 2.3 Radio: GBI and Ryle Telescope

Dataset 1 includes two GBI data points and dataset 2 includes a data point from Ryle Telescope. Lightcurves from these telescopes are shown in Figures 2 and 3, respectively.

For the GBI data, a flux density calibration procedure similar to that reported in Waltman et al (1994) has been employed here. The flux densities of 0237-233, 1245-197, and 1328+254 were determined using observations of 1328+307 (3C 286). The flux density of 3C 286 was based on the scale of Baars et al. (1977), and the assumed values were 11.85 Jy at 2.25 GHz and 5.27 Jy at 8.3 GHz<sup>2</sup>. On MJD 51367.371 the GBI flux densities were  $25 \pm 4$  mJy at 2.25 GHz and  $30 \pm 6$  mJy at 8.3 GHz. Similar behaviour was shown during a plateau state of April 2000 (Ueda et al. 2002).

<sup>1</sup> <http://www.eso.org/sci/facilities/paranal/instruments/isaac/tools/lib/>

<sup>2</sup> <http://www.gb.nrao.edu/fgdocs/gbi/plgbi/README>

The Ryle Telescope operates at 15 GHz and it observed GRS 1915+105 (simultaneously with ObsID 90105-07-02-00) from MJD 53473.098 to MJD 53473.417. The data used here are from Rodriguez et al. (2008a) and were reduced following Pooley & Fender (1997); observations of Stokes I+Q were interwoven with those of a nearby phase calibrator (B1920+154). The flux-density scale was set by reference to 3C48 and 3C286, and should be consistent with that defined by Baars et al. (1977).

On MJD 53473 we see the average radio flux density increasing from  $44.9 \pm 3.0$  to  $70.4 \pm 4.3$  mJy (Rodriguez et al. 2008b), in addition to the IR lightcurve also suggesting that in spite of the HID classification, GRS 1915+105 may not have strictly been in a plateau state. For this dataset we therefore use the average from MJD 53473.098 to 53473.25 of  $44.9 \pm 3$  mJy, closest to the RXTE and CTIO observations.

### 3 CONSTRAINTS ON INPUT PHYSICAL PARAMETERS

In order to meaningfully compare broadband spectra, we will fit our datasets using a model designed for simultaneous radio through X-ray datasets. Historically the modelling of BHBs has focused on accretion flow models of only the X-ray emission, of which Comptonising corona models have been particularly successful. However in recent years, the evidence is mounting that the bipolar jet outflows found in the HS contribute significantly across the broadband continuum. For bright transients, e.g. Russell et al. (2006, 2010) estimate up to 90% of the NIR and up to 100% in the X-rays could be dominated by jet production. Other observations of radio/IR/X-ray correlations (Corbel et al. 2000, 2003; Coriat et al. 2009) can be interpreted by either synchrotron or synchrotron-self Compton (SSC) processes relating to the jets. The outflow-dominated model of Markoff, Nowak, & Wilms (2005) (hereafter: MNW05) is still the only model that can fit the X-ray spectrum with the same precision as corona-only models (ibid; Nowak et al., in prep.) while also fitting the radio through IR bands from the same physical picture. The MNW05 model has already been applied successfully to many Galactic sources in the ‘‘canonical’’ HS: the original paper features fits to Cyg X-1 and GX 339-4, while a different data set of the latter, along with observations of XTE J1118+480 are fit in Maitra et al. (2009). Further papers have explored applications to simultaneous broadband data sets from GRO J1655-40 and A0620-00 (Migliari et al. 2007; Gallo et al. 2007), with other sources in progress. The results of all these applications has been the discovery, perhaps not surprisingly, that the free parameters fit into similar ranges for all stellar mass sources.

Furthermore, the discovery of a Fundamental Plane of black hole accretion (Merloni, Heinz, & di Matteo 2003; Falcke, K rding, & Markoff 2004) supports mass-scaling accretion physics from stellar to supermassive BHs, and thus would argue that the MNW05 should also apply to weakly accreting AGN. Confirming this, Markoff et al. (2008) successfully fit several spectral energy distributions (SEDs) from the supermassive BH M81\* with parameters in the ranges found from BHBs.

There exists, therefore, a solid framework for the modelling of BHBs in the canonical HS, against which to test

fits of data from the GRS 1915+105 plateau state. In this paper we do not consider whether MNW05 is correct but rather use it as a benchmark to test how far GRS 1915+105 fits the phenomenology of the hard state.

Whenever possible, we fixed values for model physical parameters in accordance with those found in other publications during the fitting process. In the following subsections, we first discuss how we obtained these values (presented in Table 2), and then briefly summarise the MNW05 model and our fitting methods before presenting our results.

#### 3.1 Distance and Hydrogen Column Density

The distance to GRS 1915+105 is still a matter of some debate. A first estimate was derived in Mirabel & Rodriguez (1994). From a core ejection they find a maximum distance of 13.7 kpc, under the assumption that the ejection was intrinsically symmetric. Rodriguez et al. (1995) attempted to derive a more accurate distance estimate by determining the kinematic distance from 21 cm absorption spectra of atomic hydrogen along the line of sight to GRS 1915+105 during a radio outburst, and find that it could be as far away as  $12.5 \pm 1.5$  kpc. Later measurements of the  $^{12}\text{CO}(J = 1 - 0)$  spectrum by Chaty et al. (1996) are consistent with this distance. They also constrain the visual extinction to be  $A_v = 26.5 \pm 1.7$  mag, corresponding to a total hydrogen column density of  $N_H = 4.7 \pm 0.2 \times 10^{22} \text{ cm}^{-2}$ .

If GRS 1915+105 resides at 12.5 kpc, it must be accreting above the Eddington limit ( $L_{X\text{-ray}} \sim 2.9 \times 10^{39} \text{ erg s}^{-1}$ ; McClintock & Remillard 2003, giving  $L_{X\text{-ray}}/L_{\text{Edd}} \sim 1.5$ , using a mass of  $14 M_\odot$ ; see next Section). A slightly lower maximum distance of  $11.2 \pm 0.8$  kpc, derived from proper motion studies of radio ejecta during four major events (Fender et al. 1999), would still give a ratio  $L_{X\text{-ray}}/L_{\text{Edd}} \sim 1.3$ .

However, this distance could be too large. Chapuis & Corbel (2004) measure  $^{12}\text{CO}(J = 1 - 0)$  velocity spectra of clouds along the line of sight, as well as of two nearby HII regions, and re-evaluate the hydrogen column density to  $N_H = 3.5 \pm 0.3 \times 10^{22} \text{ cm}^{-2}$ . This column gives a visual extinction of  $A_v = 19.6 \pm 1.7$  mag, reducing the number intervening molecular clouds, and arguing for a smaller distance to GRS 1915+105 of  $9.0 \pm 3.0$  kpc (at 9 kpc the accretion rate estimate drops below Eddington), based on evidence that GRS 1915+105 lies behind the molecular hydrogen cloud G 45.45+0.06. This cloud is at  $\sim 7$  kpc (Feldt et al. 1998), however Chapuis & Corbel (2004) suggest that this cloud belongs to a huge complex, located at a distance of 6 kpc, providing the above *lower* limit to the distance (the upper limit of 12 kpc is from Fender et al. 1999). However, the high column density required (Mirabel & Rodriguez 1994; Rodriguez et al. 1995) suggests that another molecular cloud should be between us, therefore Fender et al. (1999) adopted the conservative distance of 11kpc.

Considering the assumptions made in Chapuis & Corbel (2004) and the resulting size of the errorbars, we have decided to follow Fender et al. (1999) in adopting a more conservative distance of 11 kpc for this work. This distance is consistent with  $N_H = 3.5 \pm 0.3 \times 10^{22} \text{ cm}^{-2}$ , which we believe is the correct value pertaining to the IR band, as well as the larger hydrogen column density of  $4.7 \times 10^{22} \text{ cm}^{-2}$  from Chaty et al. (1996), that we use for our X-ray fits, motivated by the works of e.g. Klein-Wolt et al. (2002) (see Section 5).

**Table 2.** Fixed physical parameters used in the fitting process, obtained from the literature. We omit the error bars, as they are not used in the fits.

| parameter         | value     | units                     | Reference |
|-------------------|-----------|---------------------------|-----------|
| column density    | 4.7       | $10^{22} \text{ cm}^{-2}$ | a         |
| mass              | 14 and 23 | $M_{\odot}$               | b         |
| inclination       | 66 and 50 | $^{\circ}$                | c         |
| distance          | 11 and 6  | kpc                       | c, d      |
| donor temperature | 4455      | K                         | e         |

References: a: Chaty et al. (1996), b: Greiner et al. (2001a), c: Fender et al. (1999), d: Chapuis & Corbel (2004), e: Alonso, Arribas, & Martínez-Roger (1999)

Because a distance of 11 kpc implies super-Eddington luminosities for GRS 1915+105, we also fit the data using the minimum distance of 6 kpc, in order to explore the importance of distance on the modelling conclusions.

### 3.2 GRS 1915+105 Black Hole Mass

In order to constrain the mass of the compact object in a binary via the mass function, the orbital period, inclination and the mass of the companion (or the mass ratio) must all be known. Greiner, Cuby, & McCaughrean (2001a) found an orbital period  $P_{\text{orb}}$  of 33.5 days and a velocity amplitude  $K=140\pm 15 \text{ km s}^{-1}$ , giving a mass function  $f(M) = 9.5 \pm 3.0 M_{\odot}$ . Assuming the binary plane is the same as that of the accretion disc, the orbital inclination can be estimated from the orientation of the jets. As no constant precession has been observed, the jets can be assumed perpendicular to the accretion disc and orbital plane. The exact inclination is however still open to debate, as it is determined from the brightness and velocities of both the approaching and receding blobs. At a distance of 11 kpc the inclination is  $i = 66^{\circ} \pm 2^{\circ}$  (Fender et al. 1999). Harlaftis & Greiner (2004) were able to deduce a mass ratio  $M_d/M_X = 0.053 \pm 0.033$  from the rotational broadening of photospheric absorption lines of the donor star. Together these values give a mass for GRS 1915+105 of  $14.0 \pm 4.4 M_{\odot}$  (Greiner, Cuby, & McCaughrean 2001a). We use these as our fiducial values for the distance and mass. For the 6kpc distance we calculate a smaller inclination of  $i = 50^{\circ}$  using Fender et al. (1999), and, using Harlaftis & Greiner (2004) a mass of  $23 M_{\odot}$ .

### 3.3 Properties of the Donor Star

A rough identification of the companion was performed by Greiner et al. (2001b), by analysing absorption line features in the NIR. They conclude that the companion is a class III K-M giant and compare it successfully to a K2 III star. If the star is indeed a K2 III giant, its temperature should be  $T_d = 4455 \pm 190 \text{ K}$  (Alonso, Arribas, & Martínez-Roger 1999), and accretion proceeds via Roche-lobe overflow (Greiner et al. 2001b). We use this temperature for the simplistic blackbody spectral component representing the companion in our spectral fits.

## 4 MODELLING AND RESULTS

### 4.1 Description of model

For all spectral fits we use the program ISIS (Houck & Denicola 2000) compiled with XSPEC version 12.3.1x libraries (Arnaud 1996). The model discussed below is forward-folded through the X-ray detector response matrices, but applied directly to the radio through NIR data. To account for the additional uncertainties in the PCA response matrix, a 0.5% systematic error has been added in quadrature to all PCA data. As the relative calibration of the PCA and HXTE instruments is not certain, the normalisation factor for the PCA data is set to unity and tied to the radio and NIR normalisations during the fits, while the HEXTE data normalisation is left free to vary.

As the focus of our paper is on modelling the non-thermal spectrum, and the exact stellar model needed for GRS 1915+105 is uncertain, we use a simple blackbody to model the NIR, with the temperature fixed as discussed in the previous Section. This component serves to account for the excess IR/optical flux level due to the star, so that the overall model normalisation is correct.

In addition to the jet and the star we have an outer accretion flow in the form of a "standard" geometrically thin accretion disc (Shakura & Sunyaev 1973). This flow is parametrised by the radius of the inner and outer disc edges ( $r_{\text{in}}, r_{\text{out}}$ ) and the temperature at the inner edge ( $T_{\text{in}}$ ). In the Schwarzschild geometry, the innermost stable circular orbit has a radius of  $6 r_g$ , but this radius can be reduced to  $1 r_g$  in the Kerr metric, when the BH is maximally spinning. The disc component serves to both fit spectral signatures of thermal emission from the accretion flow in the X-ray band, as well as contributing seed photons for inverse Compton scattering, but is only a weak element in comparison to the entire spectrum.

We now summarise the physical parameters in our jet (see Table 3). One of the most important of these parameters is the jet luminosity ( $N_j$ ). This factor scales with the accretion power at the inner edge of the accretion disc and represents the power going into the jet and acts as a normalisation factor. The power is equally divided to supply the internal and kinetic pressures. We assume that the kinetic energy is carried by cold protons, while the leptons do the radiating. The energy involved in the internal pressure goes into the particle and magnetic energy densities, with a ratio determined by  $k$ .  $k = 1$  equals equipartition and higher values indicate magnetic dominance. The initial velocity at the base of the jet, or "nozzle" is the proper sound speed of an electron/proton plasma:  $\beta\gamma c \sim 0.4c$ . The radius of the jet-base is also a free parameter,  $r_0$  (expressed in in units of gravitational radius  $r_g = GM/c^2$ ). The particles start of in a quasi-thermal (relativistic) Maxwellian distribution, the peak energy of which is determined by the electron temperature ( $T_e$ ). Beyond the nozzle the jet is allowed to expand freely, or adiabatically, causing a longitudinal pressure gradient. This pressure gradient leads to a moderate acceleration of the jet along the direction of flow; the resulting velocity profile is calculated from the Euler equations and is roughly logarithmic, evening out at bulk speeds with Lorentz factors of  $\Gamma \sim 2 - 3$  (see e.g. Falcke, Markoff, & Bower 2009). In a segment of the jet located at some variable distance ( $z_{\text{acc}}$ ; also expressed in  $r_g$ ) from the base, we assume a significant

fraction (75 %) of the leptons is accelerated into a power-law. The slope of the power-law particle distribution  $p$  is also not pre-determined. In each jet segment after the acceleration front, the general shape of the distribution is assumed to remain the same, while the total lepton density decreases according to the adiabatic expansion. This is achieved assuming a continuous injection of “fresh” energetic power-law distributed electrons ( $N(E)dE \propto E^{-p}dE$ ) in each segment after the acceleration region. The jet is stopped at a distance  $z_{\max}$  from the base.

All fits are done using the following components: (1) The MNW05 steady-state outflow-dominated model that includes a multi-colour blackbody accretion disc and a single blackbody for the companion star; (2) an additive **Gaussian** line profile, with a line energy left free to vary between 6 and 7 keV, and line width  $\sigma$  free to vary between 0 and 2 keV; Models (1)+(2) are either convolved with Compton reflection from a neutral medium (**reflect**; Magdziarz & Zdziarski 1995) or multiplied with the smeared edge model (**smedge**; Ebisawa 1991; using the “standard” index for the photoelectric cross-section of  $\sim -2.67$ ), that accounts for relativistic smearing of the iron line, and multiplied with a photo-electric absorption model (**phabs**) to account for the interstellar medium. As the strength of an absorption feature (or edge) is related to the strength of the according emission line, the line width is in principle also related to the absorption edge width. Thus when using the **smedge** model, we tie the width of the edge to the width of the **Gaussian**. For the **reflect** model we assume the viewing angle to correspond to the jet inclination. Furthermore, although the **reflect** model already includes an absorption edge, it is a sharp un-smearred edge, therefore we also tried fitting the data with both the **smedge** and **reflect** models.

## 4.2 Spectral fitting and results

The results of all fits are presented in Figures 6–11, with respective parameters listed in Table 3. Below we discuss the individual fits to both datasets in more detail.

Initial fits revealed that, in the case of GRS 1915+105, using **smedge** is statistically preferred to using **reflect**, to model the reflection features above  $\sim 10$  keV. Therefore, we proceed to fit the data in greater detail with the **smedge** model, but include a fit that employs **reflect** as this model has been used generally to model the disc reflection in previous works (see Section 3).

The spectral index of the optically thick radio-NIR synchrotron emission is determined in part by the internal jet plasma parameters such as the electron temperature, but it is most sensitive to the Doppler beaming factor (calculated from the inclination of the jets). The closer the jet axis aligns with the line of sight, the less inverse the observed radio spectrum. Fixing the inclination according to observation and choosing a jet length for all fits of  $10^{16}$  cm, sufficient so that the slope through the radio data points is continuous, reveals a key difference between the two GRS 1915+105 plateau state datasets and canonical BHBs. In order to avoid too much excess in the NIR over the companion star BB, and to provide the best NIR fit, the initial particle acceleration region in the jets  $z_{\text{acc}}$  needs to be at a distance of at least  $\sim 10^4 r_g$ . Therefore the post-acceleration region in the jets does not dominate the X-ray emission below  $\sim 10$

keV, in contrast to canonical BHBs in the hard state where acceleration is found to begin on the order of 10s of  $r_g$ .

In general we obtain values for electron energy index  $p \sim 2.2$  that result in a significant synchrotron contribution to the X-rays below  $\sim 20 - 50$  keV, with a ratio of synchrotron to inverse Compton flux of  $\sim 0.1$ . The steeply declining X-ray flux above  $\sim 20$  keV is best fit by a dominant inverse Compton contribution from the base of the jets. With a much harder value of  $p$  we could conceivably fit more of the X-ray emission via synchrotron emission, but only if the exponential decay shape plays a significant role (see Figure 11 for such a fit to dataset 2). For very soft values of the spectral index, synchrotron emission will not contribute significantly, but fits without any synchrotron contribution to the X-ray at all are not statistically favoured.

The exact spectral shape and normalisation in the post-acceleration synchrotron component (fitting the radio data) are very dependent on the value of  $p$ . When calculating a local statistical minimum, the fitting routine naturally favours the plethora of X-ray data points over the few radio data points, in finding the confidence limits for  $p$ , explaining non-negligible systemic residuals in the radio.

For clarity we note that below we will use **SMALL CAPS** to refer to fits and will continue to use the **typewriter** font to refer to models.

### 4.2.1 Dataset 1

The best fit models for dataset 1 are shown in Figures 6 - 9 (corresponding to Table 3, **SMEDGE**, **REFLECT**, **SMEDGE2** and **6KPC** column respectively; see below for explanation of these fit names). The fits are in general statistically good, with a large contribution to the residuals coming from the inadequacy of a simple black body to fit the NIR data (see Figure 5). Completely removing the NIR data from the best fit **SMEDGE** models an improvement in the  $\Delta\chi_{\text{red}}^2$  of  $\sim 0.08$ , to  $\chi_{\text{red}}^2 = 0.69$ .

Our best fit **SMEDGE**, employing the **smedge** model also shows the most extreme behaviour in terms of the distribution of the energy budget (evident from the value for the magnetic dominance  $k$ ) and the acceleration front distance  $z_{\text{acc}}$ . In addition this fit is likely to suffer from pair production (see Table 4 and Section 5). Hence we explore several fits with less extreme physical properties, including two more fits employing a **smedge** model, (**SMEDGE2** and **6KPC**) and one fit using the **reflect** model (**REFLECT**). The **SMEDGE** and **SMEDGE2** fits are different local minima that primarily differ from each other in the distribution of the energy budget, most importantly the latter fit has a reduced value for the magnetic dominance  $k$  and particle distribution index  $p$ . For **6KPC** we reduced the distance to GRS 1915+105 to 6 kpc (see below). These fits clearly show over an order of magnitude decrease in  $z_{\text{acc}}$  and a factor 2 – 25 reduction in  $k$ . Moreover, pair production will be less important. We note here that fixing  $z_{\text{acc}}$  to  $2 \times 10^4 r_g$  in the **SMEDGE** fit results in only a minor increase in  $\chi_{\text{red}}^2$  of 0.05, while producing virtually the same model parameters. This suggests that in this case our model does not converge and shows artefacts from the fitting routine that tries to find the absolute local minimum (within the tolerance limit), although there is no real physical basis for this insignificant improvement. Hence for

**Table 3.** Parameter ranges found in canonical black holes GX339-4 (Markoff et al. 2005; Maitra, Markoff & Brocksopp 2009), XTE J1118+480 (Maitra, Markoff & Brocksopp 2009), Cyg X-1 (Markoff et al. 2005), GRO J1655-40 (Migliari et al. 2007) and A0620-00 (Gallo et al. 2007), during the HS and best-fit parameters for the GRS 1915+105 plateau state. The error bars have been resolved at 90 percent confidence level. We failed to resolve the error bars for parameters listed in italics.  $N_j$  is the jet normalisation,  $r_0$  the nozzle radius,  $T_e$  the temperature of the leptons as they enter the jet,  $p$  the spectral index of the radiating particles,  $k$  the ratio between magnetic and electron energy densities,  $z_{acc}$  location of the particle acceleration region in the jet,  $f_{scat}$  0.36/ ratio between scattering mean free path and gyroradius,  $L_{disc}$  and  $T_{disc}$  the luminosity and temperature of the accretion disc,  $A_{HXT}$  is the relative normalisation between HEXTE and PCA,  $A_{line}$ ,  $E_{line}$  and  $\sigma$  are the normalisation, the energy and width of the iron line feature, and  $E_{edge}$  and  $\tau_{max}$  are the energy and the normalisation of the **smedge** model iron line edge (the iron edge width is the same as that of the **Gaussian**) and  $\Omega/2\pi$  is the reflection fraction from the **reflect** model.

| variable        | units             | range found<br>in canonical<br>BHBs | GRS 1915+105                            |   |   |  |   |  |
|-----------------|-------------------|-------------------------------------|---|---|---|--|---|--|
|                 |                   |                                     | MJD 51367                               |   |   |  | MJD 53473                               |  |
|                 |                   |                                     | SMEDGE                                  | REFLECT                                 | SMEDGE2                                 | 6KPC                                   | ELTEMP                                  | SYNCH                                  |
| $N_j$           | $10^{-1}L_{Edd}$  | 0.0034 - 0.71                       | 4.78 <sup>+0.01</sup> <sub>-0.00</sub>  | 6.45 <sup>+0.00</sup> <sub>-0.01</sub>  | 9.91 <sup>+0.01</sup> <sub>-0.00</sub>  | 2.22 <sup>+0.01</sup> <sub>-0.01</sub> | 13.65 <sup>+0.00</sup> <sub>-0.41</sub> | <i>1.99</i>                            |
| $r_0$           | $GM/c^2$          | 3.5 - 20.2                          | 20.39 <sup>+0.01</sup> <sub>-0.01</sub> | 9.30 <sup>+0.01</sup> <sub>-0.00</sub>  | 6.45 <sup>+0.00</sup> <sub>-0.00</sub>  | 4.94 <sup>+0.05</sup> <sub>-0.01</sub> | 4.18 <sup>+0.24</sup> <sub>-0.15</sub>  | 3.6 <sup>+0.6</sup> <sub>-0.6</sub>    |
| $T_e$           | $10^9$ K          | 20 - 52.3                           | 9.21 <sup>+0.00</sup> <sub>-0.01</sub>  | 7.70 <sup>+0.01</sup> <sub>-0.00</sub>  | 8.45 <sup>+0.00</sup> <sub>-0.00</sub>  | 9.01 <sup>+0.06</sup> <sub>-0.01</sub> | 3.94 <sup>+0.00</sup> <sub>-0.02</sub>  | 8.38                                   |
| $p$             |                   | 2.1 - 2.9                           | 2.30 <sup>+0.05</sup> <sub>-0.06</sub>  | 2.10 <sup>+0.03</sup> <sub>-0.05</sub>  | 1.84 <sup>+0.01</sup> <sub>-0.00</sub>  | 2.53 <sup>+0.06</sup> <sub>-0.04</sub> | 2.14 <sup>+0.08</sup> <sub>-0.03</sub>  | 1.16 <sup>+0.03</sup> <sub>-0.03</sub> |
| $k$             |                   | 1.1 - 7                             | 692 <sup>+1</sup> <sub>-1</sub>         | 270 <sup>+1</sup> <sub>-1</sub>         | 28.9 <sup>+0.0</sup> <sub>-0.1</sub>    | 95 <sup>+2</sup> <sub>-3</sub>         | 707 <sup>+68</sup> <sub>-265</sub>      | 200                                    |
| $z_{acc}$       | $10^3 GM/c^2$     | 0.007 - 0.4                         | <i>844</i>                              | <i>30</i>                               | 20 <sup>+4</sup> <sub>-1</sub>          | <i>7.4</i>                             | <i>9</i>                                | <i>17</i>                              |
| $\epsilon_{sc}$ | $10^{-4}$         | 1.6 - 299                           | <i>0.48</i>                             | <i>0.91</i>                             | 0.87 <sup>+0.02</sup> <sub>-0.03</sub>  | <i>1.7</i>                             | <i>0.75</i>                             | 0.90 <sup>+0.22</sup> <sub>-0.19</sub> |
| $r_{in}$        | $GM/c^2$          | 0.1-486                             | 2.54 <sup>+0.00</sup> <sub>-0.06</sub>  | 2.91 <sup>+0.02</sup> <sub>-0.02</sub>  | 4.67 <sup>+0.04</sup> <sub>-0.06</sub>  | 0.62 <sup>+0.00</sup> <sub>-0.01</sub> | 4.32 <sup>+0.53</sup> <sub>-0.54</sub>  | 3.6 <sup>+0.5</sup> <sub>-0.5</sub>    |
| $L_{disc}^b$    | $10^{-1} L_{Edd}$ | 0.007 - 0.99                        | 0.91                                    | 1.26                                    | 1.51                                    | 0.73                                   | 2.49                                    | 1.82                                   |
| $T_{disc}$      | keV               | 0.06 - 1.53                         | 0.86 <sup>-0.00</sup> <sub>-0.01</sub>  | 0.83 <sup>+0.00</sup> <sub>-0.00</sub>  | 0.68 <sup>+0.01</sup> <sub>-0.00</sub>  | 0.88 <sup>+0.02</sup> <sub>-0.05</sub> | 0.81 <sup>+0.03</sup> <sub>-0.04</sub>  | 0.82 <sup>0.04</sup> <sub>-0.06</sub>  |
| $A_{HXT}$       |                   | -                                   | 0.91 <sup>+0.01</sup> <sub>-0.01</sub>  | 0.91 <sup>+0.00</sup> <sub>-0.01</sub>  | 0.92 <sup>+0.00</sup> <sub>-0.01</sub>  | 0.91 <sup>+0.01</sup> <sub>-0.01</sub> | 0.90 <sup>+0.01</sup> <sub>-0.01</sub>  | 0.90 <sup>+0.02</sup> <sub>-0.01</sub> |
| $A_{line}$      | $10^{-3}$         | -                                   | 37 <sup>+5</sup> <sub>-2</sub>          | 80 <sup>+3</sup> <sub>-2</sub>          | 48 <sup>+2</sup> <sub>-2</sub>          | 29 <sup>+2</sup> <sub>-2</sub>         | 28 <sup>+8</sup> <sub>-4</sub>          | 25 <sup>+6</sup> <sub>-3</sub>         |
| $E_{line}$      | keV               | -                                   | 6.31 <sup>+0.10</sup> <sub>-0.05</sub>  | †6.00 <sup>+0.06</sup> <sub>-0.00</sub> | †6.00 <sup>+0.04</sup> <sub>-0.00</sub> | 6.34 <sup>+0.09</sup> <sub>-0.12</sub> | 6.35 <sup>+0.09</sup> <sub>-0.09</sub>  | 6.36 <sup>0.09</sup> <sub>-0.09</sub>  |
| $\sigma$        | keV               | -                                   | 0.81 <sup>+0.10</sup> <sub>-0.06</sub>  | 1.32 <sup>0.05</sup> <sub>-0.05</sub>   | 0.92 <sup>+0.06</sup> <sub>-0.07</sub>  | 0.67 <sup>+0.17</sup> <sub>-0.14</sub> | <i>0.22</i>                             | <i>0.07</i>                            |
| $\Omega/2\pi$   |                   | 0.00 - 0.35                         | -                                       | †0.30 <sup>+0.00</sup> <sub>-0.01</sub> | -                                       | -                                      | -                                       | -                                      |
| $E_{edge}$      | keV               | -                                   | 9.15 <sup>+0.15</sup> <sub>-0.11</sub>  | -                                       | 8.87 <sup>+0.14</sup> <sub>-0.13</sub>  | 9.08 <sup>+0.18</sup> <sub>-0.16</sub> | 9.09 <sup>+0.25</sup> <sub>-0.16</sub>  | 9.13 <sup>+0.22</sup> <sub>-0.25</sub> |
| $\tau_{max}$    | $10^{-2}$         | -                                   | 12 <sup>+1</sup> <sub>-2</sub>          | -                                       | 19 <sup>+1</sup> <sub>-1</sub>          | 12 <sup>+1</sup> <sub>-2</sub>         | 11 <sup>+2</sup> <sub>-2</sub>          | 10 <sup>+1</sup> <sub>-2</sub>         |
| $\chi^2/DoF$    |                   |                                     | 113/147<br>(=0.77)                      | 150/148<br>(=1.02)                      | 166/147<br>(=1.13)                      | 131/147<br>(=0.89)                     | 59/81<br>(=0.73)                        | 59/81<br>(=0.73)                       |

### MNW05 Canonical Parameter Ranges and GRS 1915+105 Best-Fit Parameters

† Value is pushing lower or upper boundary and is therefore not well constrained.

<sup>b</sup> Derived from model values for  $r_{in}$  and  $T_{disc}$ .

the SMEDGE fit we will ignore the value for  $z_{acc}$  but include the other parameter values in our analysis.

The steeper optically thin synchrotron spectrum of SMEDGE2 could be reconciled with the steeper  $p$  found in canonical BHBs by assuming that both share such a hard injected power-law, and considering the effect of cooling on the spectrum. We do not consider cooling explicitly here, but are investigating such issues in a separate work. Because of the diminishing magnetic field strength along the jets, the cooling (dominated by synchrotron losses) is negligible. The break energy where the particle distribution steepens in “particle space” shifts according to  $E \propto B^{-2} \propto r^2$  (Kardashev 1962). Thus the further along the jet we go, the less important cooling becomes, and thus the largest contribution to the higher frequencies from synchrotron radiation is from the first acceleration zone. Because this zone occurs almost two orders of magnitude further out in GRS 1915+105 compared to BHBs, this effect could explain why we are seeing the uncooled injected spectrum rather than the cooled spectrum, expected to be steeper by 0.5.

From the arguments outlined in the previous Section it

is clear that the true distance to GRS 1915+105 could be much smaller than the 11 kpc adopted for most of our fits. In an attempt to explore the effect of distance, we performed one fit on dataset 1 with the distance to GRS 1915+105 reduced to 6 kpc (see Figure 9 and Table 3, 6KPC column). The modifications result in a similar  $\chi^2_{red}$  but some values are closer to what we have come to expect for the HS in other black holes. Firstly we find  $z_{acc}$  to be the smallest of all fits. This can be understood from the smaller inclination of  $50^\circ$  corresponding to the smaller distance, resulting in a less inverse radio spectrum and hence a lower flux level at the IR break. In addition the jet luminosity  $N_j$  and the partition parameter  $k$  are closer to values found for other BHBs. With  $N_j \sim 0.22L_{Edd}$  and  $k \sim 90$  they are only a fraction of the values found for most 11 kpc fits. Also the smaller nozzle radius  $r_0 \sim 5$  is more typical of the usual HS value. One possible interpretation of these results is that GRS 1915+105 might in fact be closer than the conservative value usually taken in the more recent literature.



#### 4.2.2 Dataset 2

The best fit models for dataset 2 are shown in Figures 10 and 11 (corresponding to Table 3, column, ELTEMP and SYNCH respectively). ELTEMP offers the best comparison – in terms of what component fits what feature – to dataset 1, and owes its name to its low electron temperature  $T_e$ , while SYNCH is dominated by the post acceleration synchrotron component.

Fitting dataset 2 with similar parameter values (relating to the energy budget and assumed geometry) as dataset 1 yields very poor statistics (best  $\chi_{\text{red}}^2 \sim 30$ ). Trying to model the steep X-ray spectrum, mainly employing the exponential decay of the multicolour disc fails, because a higher disc contribution offers more (soft) seed photons. These photons are up-scattered and create a Compton tail in the hardest part of the spectrum where they overestimate the observed flux.

We therefore searched the parameter space for any other solution that reduces the flux of Comptonised high-energy photons by reducing the electron temperature  $T_e$ . A lower temperature electron distribution would on average not up-scatter the disc seed photons to equally high energy. We find that if we allow  $T_e$  to evolve freely, we end up with a very good fit ( $\chi_{\text{red}}^2 \sim 0.7$ ), however the final temperature is rather low. At  $\sim 4 \times 10^9$  K the bulk of the electrons would be sub-relativistic. The use of a relativistic Maxwell-Jüttner distribution, as done in the MNW05 model, would no longer be fully justified, as the majority of the particles in the thermal distribution would have  $\gamma = 1$ . However this approach effects a very peaked and steep pre-shock synchrotron component. This distribution of seed jet-base photons allows for a Comptonised photon distribution that is steep enough to fit the X-ray data up to 50 keV. Above 50 keV the Comptonised disc photons harden the model spectrum just enough to fit the entire range of HEXTE data.

An alternate possibility for fitting dataset 2 - with an increased electron temperature - is found when we increase the ratio of synchrotron to inverse Compton emission. With synchrotron dominating below  $\sim 30$  keV (see Figure 11 and Table 3, SYNCH column) and cutoff at about 1 keV, the subsequent exponential decay can approximate the X-ray features rather well, when combined with an accretion disc peaking at the same energy (Figure 11). In general we feel that, given the unknowns in the exact shape of the particle distribution around the cutoff, it is undesirable to rely on this in general during the fits. However it is worth noting that it provides a very good description of the data ( $\chi_{\text{red}}^2 \sim 0.7$ ). Fitting with the synchrotron cutoff requires a very hard synchrotron spectrum ( $\Gamma \sim 1.2$ ). Normally such a hard spectral index would be expected only in ultra-relativistic sources (e.g. Heavens & Drury 1988). As for the SMEDGE2 fit, the relatively shallow spectrum could, however, again be (partly) reconciled with the canonical values for  $p$ , considering the effect of cooling on the spectrum.

#### 4.3 Stellar companion spectrum

While the predominant temperature of a K2 star is 4455K, the dataset 1 fits show a systemic discrepancy that could be resolved increasing the blackbody temperature (and normalisation). While the temperature of 4455 K is the predomi-

**Table 4.** Relative importance of pair production processes at the base of the jet, for the statistically good fits in table 3.  $n$  is the lepton number density per  $\text{cm}^{-3}$ ,  $\dot{n}_{\text{pa}}$  and  $\dot{n}_{\text{pp}}$  are the pair annihilation rate and production rate per  $\text{cm}^{-3}\text{s}^{-1}$ , respectively. In order to compare the production rates to the lepton density, they have been multiplied by an estimate for the *residence time*, given by  $r0/c$ . If  $n \gg \text{Max}(\dot{n}_{\text{pa}}, \dot{n}_{\text{pp}})$ , and  $\dot{n}_{\text{pa}} > \dot{n}_{\text{pp}}$  we should be safe from pair production. From these two considerations, the former is the most important.

| fit     | $r0$ in $r_g$ | $\log(n)$ | $\log(\dot{n}_{\text{pa}} \times r0/c)$ | $\log(\dot{n}_{\text{pp}} \times r0/c)$ |
|---------|---------------|-----------|---|---|
| SMEDGE  | 20            | 15.3      | 12.9                                    | 15.0                                    |
| REFLECT | 9.3           | 16.1      | 14.3                                    | 15.7                                    |
| SMEDGE2 | 6.4           | 16.6      | 15.1                                    | 15.8                                    |
| 6KPC    | 4.9           | 16.0      | 14.9                                    | 15.1                                    |
| ELTEMP  | 4.2           | 17.1      | 16.3                                    | 13.4                                    |
| SYNCH   | 3.6           | 16.4      | 14.5                                    | 15.2                                    |

nant value for a solitary class 2 star of this type, clearly this is not the case for the companion of GRS 1915+105.

Although the physical properties of stars under these conditions are still largely undetermined, Kaper (2001) resolved discrepancies in the effective temperatures of donor stars in high mass X-ray binaries, of 10-25% higher than expected from their spectral classification. Increasing the temperature of our blackbody by 25% to 5500 K results in an insignificant improvement in fit by  $\Delta\chi_{\text{red}}^2 = 0.03$ .

Letting the temperature and normalisation of the blackbody in our best-fit result SMEDGE free to vary improves the  $\chi_{\text{red}}^2$  to  $81/165 = 0.5$ , but yields an extremely high blackbody temperature of  $1.33_{-0.04}^{+0.14} \times 10^5$  K. Such an exceedingly high temperature indicates that other IR contributions than photospheric emission from the secondary are likely. Chaty et al. (1996) already concluded the same from the rapid variations and spectral shape they observed in this band. In particular irradiation of the companion star and/or the disc for a source as bright as GRS 1915+105 should be quite significant, but the former is not accounted for in detail in our modelling, while the latter is not accounted for at all. Using an irradiated disc+jet model, Maitra et al. (2009) obtained disc temperatures for XTE J1118+480 in the order of a few tens of thousands Kelvin, in agreement with e.g. Hynes et al. (2006). Our obtained temperature of  $\sim 1.3 \times 10^5$  K seems rather high, however XTE J1118+480 accretes at rates  $\lesssim 10\% L_{\text{Edd}}$ , while for GRS 1915+105 this is  $\sim L_{\text{Edd}}$ . Other possibilities for IR contributions include optically thick free-free emission (although usually not observed at such high energies), or optically thin free-free radiation from an X-ray driven accretion disc wind (Fuchs, Mirabel, & Claret 2003a; Castro-Tirado, Geballe, & Lund 1996).

## 5 DISCUSSION

Clearly, and perhaps surprisingly, there are large differences between datasets 1 and 2, both in the  $\chi$  state of GRS 1915+105. While dataset 1 can be fit fairly well by the same model as for BHBs, dataset 2 is marginal, thus they do not seem to represent a standard class of spectral behaviour. Interestingly, Rau & Greiner (2003) also find significant variety between the individual  $\chi$  states they observed

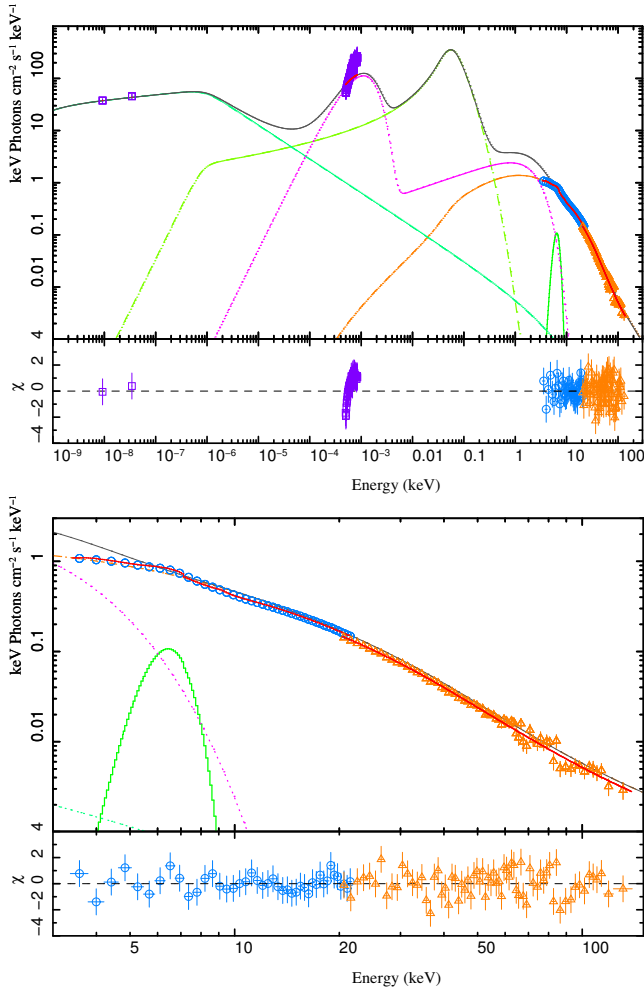


**Figure 6.** Multi-wavelength (top) and X-ray band only (bottom) best fit ( $\chi_{\text{red}}^2 \sim 1.16$ ) model spectrum (cf. Table 3, SMEDGE column), using MNW05+Gaussian+smedge. Individual contributions from the MNW05 model are also shown: The light-green dashed curve is the pre-shock synchrotron contribution. The dark-green dash-dotted curve is the post-shock synchrotron. The purple dotted curve represents the thermal contributions from the stellar blackbody (below  $\sim 10^{-2}$  keV) and the accretion disc. The orange dashed-dotted line above  $\sim 10^{-3}$  keV represent the Compton-upscattered stellar blackbody and accretion disc seed photons and the Synchrotron Self-Comptonisation (SSC) of the pre-shock synchrotron. The solid grey line is the total MNW05 model spectrum originating from the jet, the accretion disc and the companion, however not forward-folded through the detector response matrices and without iron line or reflection contributions or absorption due to the interstellar hydrogen column density or the smedge model. The red solid lines through the data points shows the model flux including all these features. The iron line complex, modelled by a Gaussian is shown by the thick green curve near 6.4 keV.

in over 4 years. While the classification done by Belloni et al. (2000) is based on lightcurves and colour-colour diagrams, the sub-indices 1-4 do not refer to a phenomenological classification scheme, but only denote their temporal sequence. Hence there remains the possibility that the  $\chi$  state still encompasses multiple physical regimes that we may be probing here via spectral fitting.

Alternately, dataset 2 could be in some kind of tran-

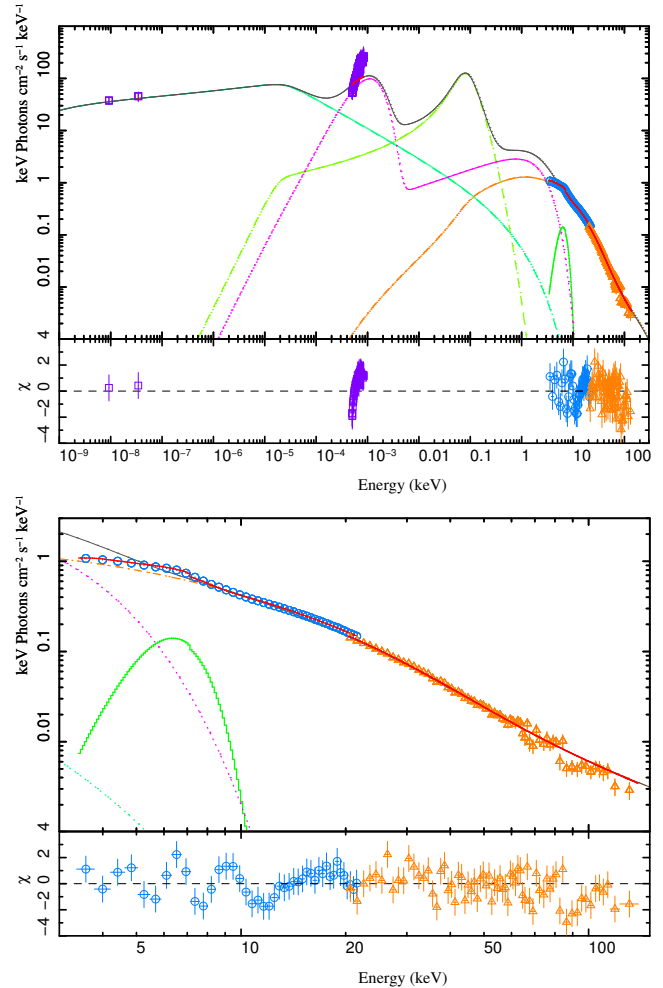


**Figure 7.** Multi-wavelength (top) and X-ray band only (bottom) best fit ( $\chi_{\text{red}}^2 \sim 1.48$ ) model spectrum (cf. Table 3, REFLECT column), using MNW05+Gaussian+reflect.

sitional state, despite being classified as a typical  $\chi$  state. In GRS 1915+105 complete state changes can happen on very short timescales in comparison to the canonical BHs (seconds). Such rapid changes generally occur only between states A and B, however. While state C episodes can also last for short periods of  $<100$  seconds, the current datasets involve only the longer (a day or more) intervals. As indicated by the radio and NIR lightcurves, it is clearly possible that during the dataset 2 observations GRS 1915+105 was in a transitional state and therefore the model, which assumes a steady outflow, is no longer applicable. Either way, both of the statistically convincing dataset 2 fits (SYNCH and ELTEMP) have other problems in their physical interpretation, as discussed above, and it is possible that the model simply cannot apply to observations at such high luminosities (see Figure 1).

For all of the fits presented, two parameters consistently stand out by nature of their larger values when compared to applications of the MNW05 model to BHBs: the location of initial particle acceleration in the jets,  $z_{\text{acc}}$ , and the energy partition parameter  $k$ . As mentioned before, we typically find  $z_{\text{acc}}$  1-2 orders of magnitude closer in towards the base of the jets in fits of other BHBs in the HS. Similarly, while

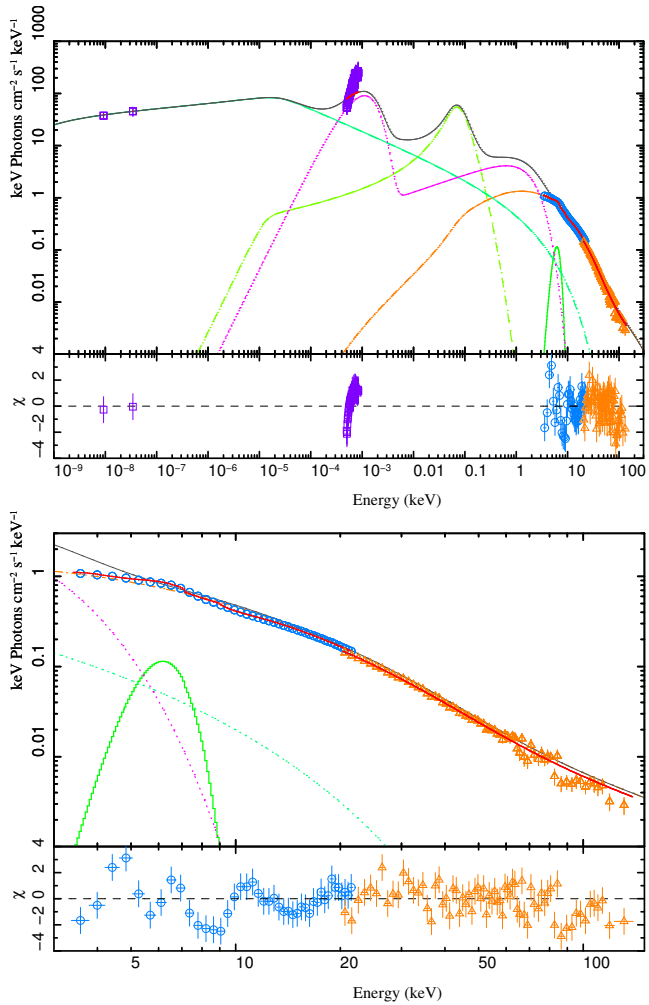


**Figure 8.** Multi-wavelength (top) and X-ray band only (bottom) best fit ( $\chi_{\text{red}}^2 \sim 1.44$ ) model spectrum (cf. Table 3, SMEDGE2 column), also employing MNW05+Gaussian+smedge, but with a reduced magnetic dominance ( $k \sim 30$  in stead of  $\sim 550$ , see table 3).

the canonical BHs often display mild magnetic domination over the gas pressure, with  $k \simeq 10$ , we find at least an order of magnitude increase is needed to fit GRS 1915+105 plateau states. Finally, the overall powers required (as indicated by the jet normalisation parameter  $N_j$ , see MNW05 for an explanation) are strikingly larger than the maximum observed in other BHs. Canonical BHs displaying these luminosity levels in  $L_{\text{Edd}}$  would long have shut down their jets, yet somehow GRS 1915+105 seems to be operating on a different energy scale.

These three parameters may well be related. Magnetic fields are by now known to play a major role in accelerating and collimating relativistic plasma outflows, and current simulations of jet formation favour rather high values of  $k$  (usually expressed as low values of the plasma  $\beta$ , denoting the ratio to of the magnetic to gas pressure; e.g. McKinney 2006; Komissarov et al. 2007; McKinney & Blandford 2009). It may be that  $k$  is positively correlated with the overall power input into the jets. Evidence for such a scaling has already been observed in individual fits to broadband data of the LLAGN M81\* over the course of a yearlong campaign

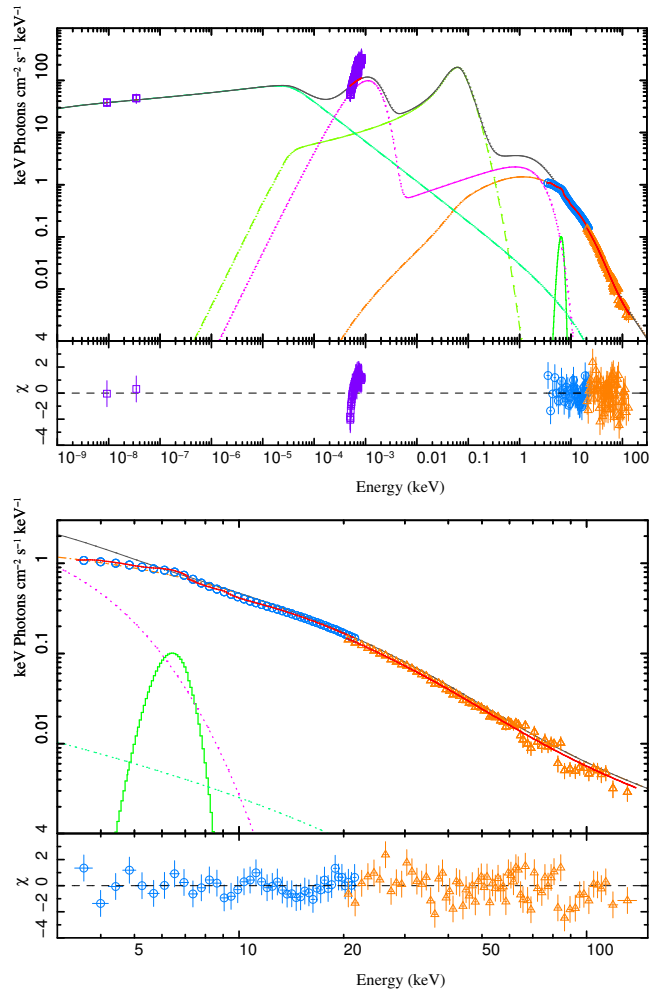


**Figure 9.** Multi-wavelength (top) and X-ray band only (bottom) best fit result ( $\chi_{\text{red}}^2 \sim 1.01$ ) spectrum (cf. Table 3, 6KPC column), for the 1999 data set, using MNW05+Gaussian+smedge and employing a fixed distance of 6 kpc.

(see, e.g. Markoff et al. 2008, Figure 22). The overall magnetic field strength and configuration will certainly influence the formation of particle acceleration structures, however the dependence on total power and other parameters has not yet been thoroughly explored.

A higher level of magnetic domination can also account for why the fits favour an electron temperature  $T_e$  that is a factor of two or more lower than the the bottom of the range ( $\sim 2 - 7 \times 10^{10}$  K) found for the canonical microquasars. A stronger magnetic field relative to the radiating plasma at the base of the jets in our model is synonymous with the same being true at the inner edge of the accretion flow, as we assume they are directly related. A relatively stronger magnetic field would result in relatively more lepton cooling in the inner regions, and consequently a lower equilibrium temperature.

In contrast, the geometry of both the base of the jets and the cool accretion disc parameters preferred in the fits is entirely consistent with the range found in the canonical BHs. The radius of the base of the jets is  $3 - 20 r_g$  exactly as seen in fits of both BHs as well as LLAGN. Similarly, we obtain best fit values for the inner cool accretion disc

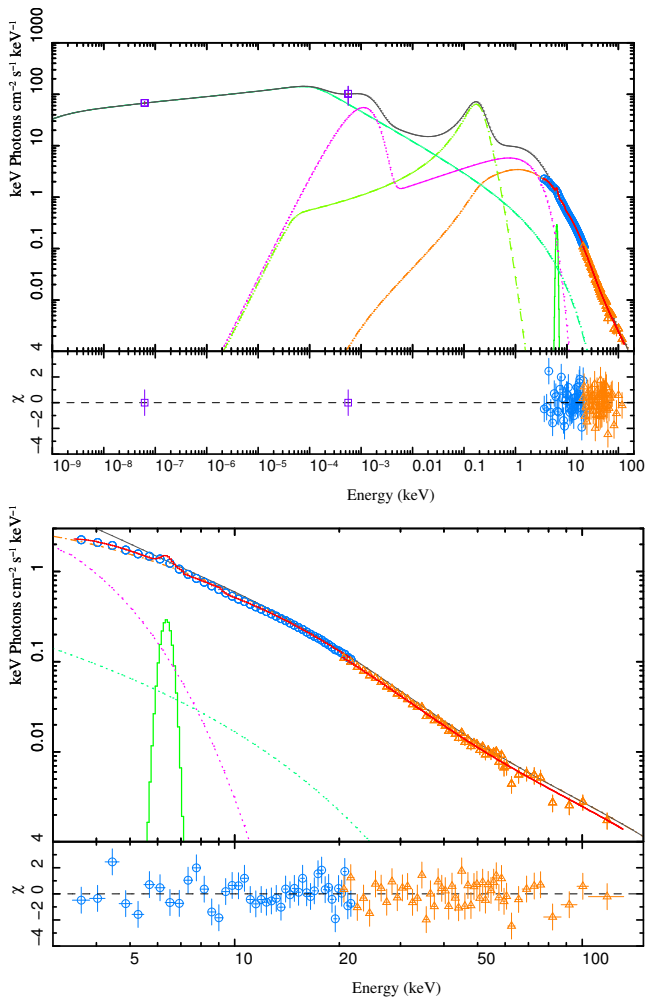


**Figure 10.** Multi-wavelength (top) and X-ray band only (bottom) best fit result ( $\chi_{\text{red}}^2 \sim 1.0$ ) spectrum, for the 2005 data set, using a reduced low electron temperature  $T_e \sim 4 \times 10^9$  K (cf. Table 3, ELTEMP column).

radius  $r_{\text{in}} \sim 2.5 - 4.7 r_g$ , which is consistent with such a high accretion rate, as well as a spinning black hole as suggested by McClintock et al. (2006). What is not consistent, and differs compared to other BHB fits, is that the jet base radius in most fits is larger (sometimes only marginally) than  $r_{\text{in}}$ . Since in our model the jets should be launched by the inner, hot accretion flow, this is not internally self-consistent and by such criteria, only fits SMEDGE2 and ELTEMP would survive. As the MNW05 model does not yet self-consistently solve the jet launching physics from a corona, which is still an unsolved problem, we have not made this a hard constraint.

Although in most BHBs such a small  $r_{\text{in}}$  would be indicative of a soft state, this is not true for GRS 1915+105. Due to the high accretion rate, a geometry where the accretion disc reaches the innermost stable orbit is almost expected. The fact that the 6KPC fit has an inner radius of less than  $1 r_g$  is most certainly due to the oversimplifications mentioned above and similar inner radii were also obtained for the canonical BHBs (see e.g. MNW05). In fact, such small radii appear to be a common occurrence, also using other models: analysing 4 years of  $\chi$  state observa-

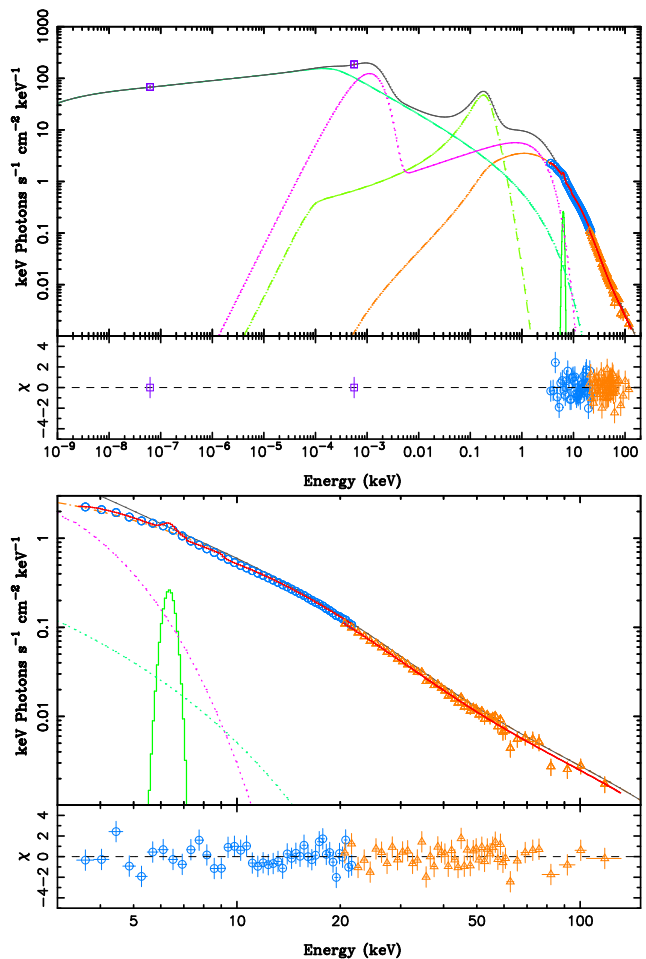


**Figure 11.** Multi-wavelength (top) and X-ray band only (bottom) best fit result ( $\chi_{\text{red}}^2 \sim 1.15$ ) spectrum, for the 2005 data set, using the synchrotron cut-off to fit the X-ray (cf. Table 3, SYNCH column).

tions Rau & Greiner (2003) obtained inner radii of far less than  $1 r_g$ , from the normalisation of the disc contribution using the `diskbb` model. Although this model is known to underestimate the inner disc radius by a factor of 1.7-3, due to Doppler blurring and gravitational redshift, the obtained radii are still unrealistically low. The disc temperatures of 1-4 keV they find are higher than ours (0.7-0.9 keV), but again the `diskbb` model is known to produce factor 1.7 overestimates (Lee et al. 2002). Comparing the two plateau states to each other, the required disc contribution is much higher in dataset 2. For dataset 1, however, disc normalisations are high but comparable to those for the canonical BHBs, suggesting that, as is true for the HS, the classification of individual plateau states should not be based on the luminosity.

In agreement with the findings of many other authors (e.g. Sobolewska & Życki 2003; Rau & Greiner 2003) who have studied the  $\chi$  state, we find that the inverse Compton component is always dominant over the direct accretion disc contribution in the X-ray regime for our datasets. Although in our case the Comptonisation is mainly due to SSC rather than purely from thermal accretion disc seed photons. Only in one dataset 2 fit (SYNCH) are the X-rays not dominated

by the Comptonisation, but the validity of this fit may be questionable on other grounds as discussed above.

As brought up as a potential issue by Maitra et al. (2009) and Malzac, Belmont, & Fabian (2009), for high luminosities conditions at the base of the jet may comprise high enough photon densities that pair production can become important. As these processes are not yet implemented in the MNW05 model, we check the pair production and annihilation rates ( $\dot{n}_{pp}$  and  $\dot{n}_{pa}$  respectively) at the base of the jets using the methods described in Maitra et al. (2009), and references therein. The results are shown Table 4. If the lepton number density  $n$  is not larger than  $\dot{n}_{pp}r_0/c$  and  $\dot{n}_{pa}r_0/c$ , where  $r_0/c$  is roughly the *residence time* for the leptons in the jet base region, we need  $\dot{n}_{pp} < \dot{n}_{pa}$  to be able to neglect pair production.

Although our  $T_e \lesssim 10^{10}$  is a factor of 5–6 lower than the limit deemed problematic for GX339-4, the extreme luminosity of GRS 1915+105 means that pair production could potentially be an issue for some of our fits. The source of potential pair production is a high-energy tail above  $\sim 0.5$  MeV, due to the Comptonisation of thermal accretion disc photons. The amount of flux in this tail is directly dependent on the normalisation and temperature of the accretion disc component, which itself is mainly constrained by the value of  $N_H$  and the predicted flux in the tail region. Higher values of  $N_H$  result in higher accretion disc fluxes to compensate for the increased absorption in the soft X-ray band.

While we fixed the value for  $N_H$  in our X-ray fits to  $4.7 \times 10^{22} \text{ cm}^{-2}$ , an increasing number of works are concluding that the column density is actually variable, ranging in values from  $N_H \sim 2 - 16 \times 10^{22} \text{ cm}^{-2}$  and potentially linked with an intrinsic warm absorber at the highest values (Belloni et al. 2000; Klein-Wolt et al. 2002; Lee et al. 2002; Yadav 2006). Although generally the column density derived from X-ray measurements is higher than those obtained using IR methods, we find that the highest values of the  $N_H$  range are not consistent with our model. Values  $\gtrsim 7$  cause too great a decrease below 3 keV, resulting in too much flux in the high-energy tail, due to enhanced disc Comptonization. We chose the above more “average” value for  $N_H$ , in order to be consistent with prior X-ray fits of the various  $\chi$  substates (e.g.  $2 \times 10^{22} \text{ cm}^{-2}$ ; Belloni et al. 1997a) and the assumptions of Chaty et al. (1996). For dataset 2 the above value is likely too high. Letting  $N_H$  free to vary (without correcting the NIR dereddening accordingly), while maintaining a higher electron temperature of  $\sim 10^{10}$  K settles on the lower bound allowed of  $2 \times 10^{22} \text{ cm}^{-2}$ , with a significant improvement in  $\chi_{\text{red}}^2$  (from  $\sim 30$  to  $\sim 25$ ), mainly due to the resulting reduction in the Comptonised high-energy tail. Therefore our results are highly dependent on the value of  $N_H$ , and that this value is likely different for the two datasets, although for the reasons described above we have chosen to use a single value. Similarly, the uncertainty in the exact value means that too much pair production can be avoided in particular by lower values of  $N_H$ . Lower values are favoured if we allow  $N_H$  to vary, and interestingly this is consistent with the conclusion by Neilsen & Lee (2009) that the presence of an absorbing disc wind at high accretion rates should be anticorrelated with the presence of jets.

## 6 CONCLUSIONS

Despite the fact that the MNW05 model was originally intended for application to hard states in canonical BHBs only, it appears to well approximate the plateau state in GRS 1915+105. However it does not produce convincing results in every instance. While some of the parameter values obtained are quite extreme, the results for the dataset 1 appear credible and consistent with what we have found in canonical BHBs. Dataset 2 however presents more difficulties, and a more solid determination of the distance and absorption column would go far to help us understand the difference between these two plateau states.

Clearly this work confirms that GRS 1915+105 is in a much more extreme range of parameter space for an outflow-dominated model, requiring near- or super-Eddington accretion rates, maximal jet powers and high levels of magnetic domination. Although our results confirm previously noted plateau state issues, such as the need for a variable  $N_H$ , our model for the first time incorporates the entire broadband and has allowed the comparison between the jet producing plateau and hard states. While the baseline geometry seems similar, the plateau states of GRS 1915+105 are not low-luminosity as with HS BHBs, and settle on a range where the acceleration of particles occurs much further out in the jets, which can be two orders of magnitude further out of equipartition in the direction of magnetic domination. While these two effects may be linked, the model explored here cannot self-consistently address this, but in another work we are exploring the links between physical parameters and the location of particle acceleration fronts (Polko et al., in prep.). A slightly lower electron temperature is also found compared to other BHBs, which can be interpreted in the context of the higher cooling rates found at GRS 1915+105’s extreme luminosity.

The main consequence of these differences is that the synchrotron component from the outer jets no longer dominates the soft X-ray band, although a non-negligible X-ray synchrotron flux of  $\sim 10$  % the inverse Compton flux below  $\sim 50$  keV seems required for the statistically favoured fits. In comparison, the MNW05 model applied to canonical BHBs favours synchrotron emission dominating the flux at least up to 10 keV. Interestingly our results are thus qualitatively similar to the results found from the blazar sequence (e.g. Ghisellini et al. 1998), where higher powers correspond to a decrease in the frequency range where synchrotron power peaks. It is clear that time-dependent effects such as cooling breaks demand further exploration, and we are currently working to implement them into more complex models.

The remarkable differences between two individual plateau state observations does raise questions about whether the  $\chi$  substates are distinct enough to classify all plateau characteristics. While both datasets explored here bear all the characteristics of the plateau state, the fits with a single model show more variations in free parameters than found even between different sources in the HS of canonical BHBs. Thus the current classification scheme based solely on X-ray colours and timing properties may need to be expanded based on broadband attributes.

Our results support a conclusion that, although expressing quite different properties than the HS in canonical BHBs, GRS 1915+105 plateau states can still be described by the

same broadband model with a steady outflow tied in power to the accretion inflow. However the BHB model is clearly forced into very extreme ranges, which themselves provide some new clues about the relationship between accretion rate, jet production and particle acceleration.

Although GRS 1915+105 is one of the most extensively studied BHBs over the last decades since its discovery, we are far from understanding this source. At some point in the future (assuming the source went into outburst when it was first discovered before the end of the century; Deegan, Combet, & Wynn 2009) GRS 1915+105 will invariably retreat into quiescence, and should finally yield better insight into the connection between its current accretion properties and those at sub-Eddington rates.

## 7 ACKNOWLEDGMENTS

The Green Bank Interferometer is a facility of the National Science Foundation operated by the NRAO in support of NASA High Energy Astrophysics programs.

SM and DM acknowledge support from a Netherlands Organization for Scientific Research (NWO) Vidi and VC Fellowship, respectively

The research leading to these results has received funding from the European Community's Seventh Framework Programme (FP7/2007-2013) under grant agreement number ITN 215212 "Black Hole Universe"

AJCT acknowledges support from the Spanish Ministry program AYA 2009-14000-C03-01

## References

- Alonso A., Arribas S., Martínez-Roger C., 1999, *A&AS*, 140, 261
- Arnaud K. A., 1996, in *Astronomical Society of the Pacific Conference Series*, Vol. 101, *Astronomical Data Analysis Software and Systems V*, Jacoby G. H., Barnes J., eds., pp. 17–+
- Baars J. W. M., Genzel R., Pauliny-Toth I. I. K., Witzel A., 1977, *A&A*, 61, 99
- Belloni T., Klein-Wolt M., Méndez M., van der Klis M., van Paradijs J., 2000, *A&A*, 355, 271
- Belloni T., Méndez M., King A. R., van der Klis M., van Paradijs J., 1997a, *ApJ*, 488, L109+
- , 1997b, *ApJ*, 479, L145
- Cardelli J. A., Clayton G. C., Mathis J. S., 1989, *ApJ*, 345, 245
- Castro-Tirado A. J., Brandt S., Lund N., 1992, *IAU Circ.*, 5590, 2
- Castro-Tirado A. J., Brandt S., Lund N., Lapshov I., Sunyaev R. A., Shlyapnikov A. A., Guziy S., Pavlenko E. P., 1994, *ApJS*, 92, 469
- Castro-Tirado A. J., Geballe T. R., Lund N., 1996, *ApJ*, 461, L99+
- Chapuis C., Corbel S., 2004, *A&A*, 414, 659
- Chaty S., 1998, PhD thesis, AA(Service d'Astrophysique, CE Saclay, France)
- Chaty S., Mirabel I. F., Duc P. A., Wink J. E., Rodríguez L. F., 1996, *A&A*, 310, 825
- Chiar J. E., Tielens A. G. G. M., 2006, *ApJ*, 637, 774
- Corbel S., 2000, in *Rossi2000: Astrophysics with the Rossi X-ray Timing Explorer*, Strohmayer T. E., ed.
- Corbel S., Fender R. P., Tzioumis A. K., Nowak M., McIntyre V., Durouchoux P., Sood R., 2000, *A&A*, 359, 251
- Corbel S., Nowak M. A., Fender R. P., Tzioumis A. K., Markoff S., 2003, *A&A*, 400, 1007
- Coriat M., Corbel S., Buxton M. M., Baylin C. D., 2009, in *American Institute of Physics Conference Series*, Vol. 1126, *American Institute of Physics Conference Series*, Rodriguez J., Ferrando P., eds., pp. 207–209
- Deegan P., Combet C., Wynn G. A., 2009, *MNRAS*, 1549
- Dhawan V., Mirabel I. F., Rodríguez L. F., 2000, *ApJ*, 543, 373
- Ebisawa K., 1991, PhD thesis, Univ. Tokyo; ISAS Research Note No. 483, (1991)
- Falcke H., Körding E., Markoff S., 2004, *A&A*, 414, 895
- Falcke H., Markoff S., Bower G. C., 2009, *A&A*, 496, 77
- Feldt M., Stecklum B., Henning T., Hayward T. L., Lehmann T., Klein R., 1998, *A&A*, 339, 759
- Fender R., Belloni T., 2004, *ARA&A*, 42, 317
- Fender R. P., Garrington S. T., McKay D. J., Muxlow T. W. B., Pooley G. G., Spencer R. E., Stirling A. M., Waltman E. B., 1999, *MNRAS*, 304, 865
- Foster R. S., Waltman E. B., Tavani M., Harmon B. A., Zhang S. N., Paciesas W. S., Ghigo F. D., 1996, *ApJ*, 467, L81+
- Fuchs Y., Mirabel I. F., Claret A., 2003a, *A&A*, 404, 1011
- Fuchs Y., Rodríguez J., Mirabel I. F., Chaty S., Ribó M., Dhawan V., Goldoni P., Sizun P., Pooley G. G., Zdziarski A. A., Hannikainen D. C., Kretschmar P., Cordier B., Lund N., 2003b, *A&A*, 409, L35
- Gallo E., Fender R. P., Pooley G. G., 2003, *MNRAS*, 344, 60
- Gallo E., Migliari S., Markoff S., Tomsick J. A., Bailyn C. D., Berta S., Fender R., Miller-Jones J. C. A., 2007, *ApJ*, 670, 600
- Ghisellini G., Celotti A., Fossati G., Maraschi L., Comastri A., 1998, *MNRAS*, 301, 451
- Greiner J., Cuby J. G., McCaughrean M. J., 2001a, *Nature*, 414, 522
- Greiner J., McCaughrean M. J., Cuby J. G., Castro-Tirado A. J., Mennickent R. E., 2001b, *Astrophysics and Space Science Supplement*, 276, 31
- Hannikainen D. C., Rodríguez J., Vilhu O., Hjalmarsdotter L., Zdziarski A. A., Belloni T., Poutanen J., Wu K., Shaw S. E., Beckmann V., Hunstead R. W., Pooley G. G., Westergaard N. J., Mirabel I. F., Hakala P., Castro-Tirado A., Durouchoux P., 2005, *A&A*, 435, 995
- Harlaftis E. T., Greiner J., 2004, *A&A*, 414, L13
- Heavens A. F., Drury L. O., 1988, *MNRAS*, 235, 997
- Homan J., Belloni T., 2005, *Ap&SS*, 300, 107
- Houck J. C., Denicola L. A., 2000, in *Astronomical Society of the Pacific Conference Series*, Vol. 216, *Astronomical Data Analysis Software and Systems IX*, Manset N., Veillet C., Crabtree D., eds., pp. 591–+
- Hynes R. I., Robinson E. L., Pearson K. J., Gelino D. M., Cui W., Xue Y. Q., Wood M. A., Watson T. K., Winget D. E., Silver I. M., 2006, *ApJ*, 651, 401
- Jahoda K., Markwardt C. B., Radeva Y., Rots A. H., Stark M. J., Swank J. H., Strohmayer T. E., Zhang W., 2006, *ApJS*, 163, 401
- Kaper L., 2001, in *Astrophysics and Space Science Library*,

- Vol. 264, The Influence of Binaries on Stellar Population Studies, Vanbeveren D., ed., pp. 125–+
- Kardashev N. S., 1962, *Soviet Astronomy*, 6, 317
- Klein-Wolt M., Fender R. P., Pooley G. G., Belloni T., Migliari S., Morgan E. H., van der Klis M., 2002, *MNRAS*, 331, 745
- Komissarov S. S., Barkov M. V., Vlahakis N., Königl A., 2007, *MNRAS*, 380, 51
- Leahy D. A., Darbro W., Elsner R. F., Weisskopf M. C., Kahn S., Sutherland P. G., Grindlay J. E., 1983, *ApJ*, 266, 160
- Lee J. C., Reynolds C. S., Remillard R., Schulz N. S., Blackman E. G., Fabian A. C., 2002, *ApJ*, 567, 1102
- Magdziarz P., Zdziarski A. A., 1995, *MNRAS*, 273, 837
- Maitra D., Markoff S., Brocksopp C., Noble M., Nowak M., Wilms J., 2009, *MNRAS*, 398, 1638
- Malzac J., Belmont R., Fabian A. C., 2009, *MNRAS*, 1453
- Markoff S., Nowak M., Young A., Marshall H. L., Canizares C. R., Peck A., Krips M., Petitpas G., Schödel R., Bower G. C., Chandra P., Ray A., Muno M., Gallagher S., Hornstein S., Cheung C. C., 2008, *ApJ*, 681, 905
- Markoff S., Nowak M. A., Wilms J., 2005, *ApJ*, 635, 1203
- McClintock J. E., Remillard R. A., 2003, *ArXiv Astrophysics e-prints*
- McClintock J. E., Shafee R., Narayan R., Remillard R. A., Davis S. W., Li L.-X., 2006, *ApJ*, 652, 518
- McKinney J. C., 2006, *MNRAS*, 368, 1561
- McKinney J. C., Blandford R. D., 2009, *MNRAS*, 394, L126
- Merloni A., Heinz S., di Matteo T., 2003, *MNRAS*, 345, 1057
- Migliari S., Tomsick J. A., Markoff S., Kalemci E., Bailyn C. D., Buxton M., Corbel S., Fender R. P., Kaaret P., 2007, *ApJ*, 670, 610
- Mirabel I. F., Rodríguez L. F., 1994, *Nature*, 371, 46
- Mirabel I. F., Rodríguez L. F., 1998, *Nature*, 392, 673
- Muno M. P., Remillard R. A., Morgan E. H., Waltman E. B., Dhawan V., Hjellming R. M., Pooley G., 2001, *ApJ*, 556, 515
- Naik S., Rao A. R., 2000, *A&A*, 362, 691
- Neil E. T., Bailyn C. D., Cobb B. E., 2007, *ApJ*, 657, 409
- Neilsen J., Lee J. C., 2009, *Nature*, 458, 481
- Pooley G. G., Fender R. P., 1997, *MNRAS*, 292, 925
- Rao A. R., Naik S., Vadawale S. V., Chakrabarti S. K., 2000, *A&A*, 360, L25
- Rau A., Greiner J., 2003, *A&A*, 397, 711
- Reig P., Belloni T., van der Klis M., 2003, *A&A*, 412, 229
- Remillard R. A., McClintock J. E., 2006, *ARA&A*, 44, 49
- Rodríguez J., Durouchoux P., Mirabel I. F., Ueda Y., Tagger M., Yamaoka K., 2002, *A&A*, 386, 271
- Rodríguez J., Hannikainen D. C., Shaw S. E., Pooley G., Corbel S., Tagger M., Mirabel I. F., Belloni T., Cabanac C., Cadolle Bel M., Chenevez J., Kretschmar P., Lehto H. J., Paizis A., Varnière P., Vilhu O., 2008a, *ApJ*, 675, 1436
- Rodríguez J., Shaw S. E., Hannikainen D. C., Belloni T., Corbel S., Cadolle Bel M., Chenevez J., Prat L., Kretschmar P., Lehto H. J., Mirabel I. F., Paizis A., Pooley G., Tagger M., Varnière P., Cabanac C., Vilhu O., 2008b, *ApJ*, 675, 1449
- Rodríguez L. F., Gerard E., Mirabel I. F., Gomez Y., Velazquez A., 1995, *ApJS*, 101, 173
- Rothschild R. E., Blanco P. R., Gruber D. E., Heindl W. A., MacDonald D. R., Marsden D. C., Pelling M. R., Wayne L. R., Hink P. L., 1998, *ApJ*, 496, 538
- Russell D. M., Fender R. P., Hynes R. I., Brocksopp C., Homan J., Jonker P. G., Buxton M. M., 2006, *MNRAS*, 371, 1334
- Russell D. M., Maitra D., Dunn R. J. H., Markoff S., 2010, *MNRAS*, 405, 1759
- Shakura N. I., Sunyaev R. A., 1973, *A&A*, 24, 337
- Sobolewska M. A., Życki P. T., 2003, *A&A*, 400, 553
- Tagger M., Varnière P., Rodríguez J., Pellat R., 2004, *ApJ*, 607, 410
- Trudolyubov S. P., 2001, *ApJ*, 558, 276
- Ueda Y., Yamaoka K., Sánchez-Fernández C., Dhawan V., Chaty S., Grove J. E., McCollough M., Castro-Tirado A. J., Mirabel F., Kohno K., Feroci M., Casella P., Trushkin S. A., Castaneda H., Kotani T., Swank J., Inoue H., 2002, *ApJ*, 571, 918
- Yadav J. S., 2006, *ApJ*, 646, 385